Trinuclear Copper(I) Complex Containing 3,4,9,10,15,16-Hexamethyl-1,6,7,12,13,18-hexaazatrinaphthylene: A Structural, Spectroscopic, and Computational Study

Samuel J. Lind, Timothy J. Walsh, Allan G. Blackman, Matthew I. J. Polson, Garth I. S. Irwin, and Keith C. Gordon*

MacDiarmid Institute for Advanced Materials and Nanotechnology, Department of Chemistry, University of Otago, Dunedin, New Zealand

Received: September 14, 2008; Revised Manuscript Received: February 15, 2009

The compound $[(Cu(PPh_3)_2)_3(HATNMe_6)](BF_4)_3$ has been synthesized and characterized by X-ray crystallography, resonance Raman spectroscopy, and density functional theory (DFT) calculations. The X-ray structure of solvated $[(Cu(PPh_3)_2)_3(HATNMe_6)](BF_4)_3$ [rhombohedral, $R\bar{3}$, $a = b = 21.6404(4)$ Å, $c = 53.188(3)$ Å, $\alpha = \beta = 90°$, $\gamma = 120°$] shows that the $HATNMe_6$ ligand is very slightly twisted. The electronic absorption spectrum of the complex in chloroform shows two bands in the visible region attributed to ligand-centered (LC) and metal-to-ligand charge-transfer (MLCT) transitions, respectively. Time-dependent DFT calculations show good agreement with experiment, with two MLCT and one LC transition predicted in the visible region (641, 540, and 500 nm). Resonance Raman spectra of the complex using discrete excitation energies between 647 and 406 nm showed a variation in enhancement patterns consistent with at least two distinct transitions. The absolute Raman cross sections have been evaluated and, through a wavepacket analysis, the amount of distortion along each vibrational mode across the Franck−Condon surface is established from the calculated dimensionless displacement (Δ) values as well as other electronic parameters. The pattern of Δ values shows good agreement with the observed calculated modes, with the MLCT transition, showing much larger Δ values for outer ring modes such as $\nu(93)$ and $\nu(205)$ than in the LC transition. This is consistent with the molecular orbitals involved in the two transitions; the donor orbitals for the LC transition have similar outer-ring bonding characteristics compared to the MLCT transition, which has no donor orbital bonding characteristics on the ligand because the donor molecular orbitals are dπ orbitals.

I. Introduction

Materials based around 1,6,7,12,13,18-hexaazatrinaphthylene (HATN) have received considerable attention in recent years due to their ability to form discotic liquid crystal phases in which the molecules form π-stacked structures. These π-stacked arrays can yield charge-carrying mobilities and as such have potential utility in molecular electronic devices.[1,2] The fact that the compounds form liquid crystals means that, in principle, they may possess a self-repair pathway, an appealing characteristic for a material placed in a device. The HATN ligands are readily reduced,[1] making them good electron carriers (n-type organic conductors). One tantalizing possibility is that HATN could be used, in concert with a p-type carrier, to create a material in which both positive and negative charges could be directed following charge-transfer excitation (Figure 1). It may be possible to use such a material in solar energy capture. Obvious candidates for hole-carrying are one or more metal ions coordinated to the HATN ligand. As a first step toward exploring this, we report a highly colored trinuclear copper(I) complex in which each of the bidentate chelate sites of 3,4,9,10,15,16-hexamethyl-1,6,7,12,13,18-hexaazatrinaphthylene, $HATNMe_6$ (Figure 2), is bound to a copper(I) bistriphenylphosphine moiety. In this work we investigate the nature of the transitions present in the visible region of the spectrum and the underlying structural distortions that photoexcitation would induce.

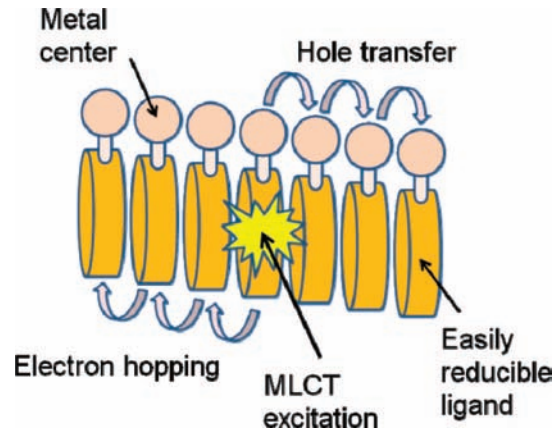

Figure 1. Charge separation scheme.

Resonance Raman spectroscopy is a very powerful technique for probing the nature of, and structural changes attendant with, photoexcitation. The resonance Raman effect causes an enhancement of Raman scattering associated with the chromophore in resonance with the excitation wavelength. The enhancement is vibrational-mode-specific in that those modes that distort the structure of the molecule to mimic the resonant electronic excitation are most strongly enhanced.[3,4] Analysis of resonance excitation profiles (plots of Raman cross section versus excitation wavelength) can yield information on the structural changes between the electronic ground state and the resonant electronic

* Corresponding author.

10.1021/jp808179m CCC: $40.75
Published on Web 03/25/2009

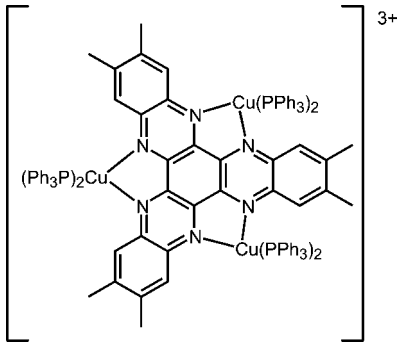

Figure 2. Complex $[(Cu(PPh_3)_2)_3(HATNMe_6)]^{3+}$ used in this study.

excited state in terms of the dimensionless displacement (Δ) along each of the vibrational normal coordinates. The wavepacket model allows for the simulation of excitation profiles and subsequent extraction of geometrical data.[5,6] This methodology has been used to examine a number of intramolecular charge-transfer systems[7−17] including metal complexes in which the MLCT transition is an active chromophore.[18−20] In very complex systems, where many overlapping bands may exist, this analysis can become unwieldy because of the delocalized nature of the normal modes and their density. However, if the nature of the vibrational modes is understood, then further insight may be gained from the Δ values. It is possible to use density functional theory (DFT) to model the vibrational modes of metal complexes with confidence that the predicted normal modes are reliable.[21−24]

The literature contains a large number of papers that have used DFT to elucidate the electronic structure of metal polypyridyl complexes. However, few of these have used frequency calculations either to validate the electronic structure methods or to understand specifically either infrared or Raman spectra. Diaz-Acosta et al.[25] used DFT implemented with the hybrid B3LYP functional and a mixed basis set comprising the standard 6-31G* basis on C, O, and H and Ahlrichs' valence triple-ζ (VTZ) on the metal atoms to examine the structure and vibrational (IR) spectra of a series of trivalent metal trisacetylacetonate complexes. They concluded that this method provided good modeling of the observed infrared spectra of these compounds. Frequency calculations have been used to interpret the spectroscopic data for the MLCT excited state of $[Re(bpy)(CO)_3(4\text{-}Etpy)]^+$ (bpy = 2,2′-bipyridine, 4-Etpy = 4-ethylpyridine) using DFT (B3LYP), with a modified LANL2DZ basis set for the effective core potential of the Re(I) center and a 6-31G* basis set for the other atoms. From this study the symmetries and normal vibrational modes for the carbonyl stretches have been established.[26−29]

We are interested in examining the properties of metal complexes with HATN ligands. Herein we report the synthesis and characterization of the trinuclear copper(I) complex $[(Cu(PPh_3)_2)_3(HATNMe_6)](BF_4)_3$ and we detail its spectroscopic and structural properties.

II. Experimental Section

$[(Cu(PPh_3)_2)_3(HATNMe_6)](BF_4)_3$. $HATNMe_6$[30] (60 mg, 0.13 mmol) was added to a suspension of $[Cu(PPh_3)_4](BF_4)$ (513 mg, 0.42 mmol) in ether (100 mL), and the white suspension turned green almost immediately. The suspension was stirred under argon at room temperature for a further 48 h and the resulting green solid was filtered off. The solid was recrystallized from methanol (15 mL). Yield 85%. Anal, Found: C, 66.09; H, 4.57; N, 3.35. Calcd for $Cu_3N_6P_6C_{138}H_{114}(H_2O)_1$: C, 66.00; H, 4.66; N, 3.35.

TABLE 1: Crystal Data and Structure Refinement for CuHATN

identification code	CuHATN	
empirical formula	$C_{96}H_{84}B_2Cl_3Cu_2F_8N_4OP_4$	
formula weight	1840.62	
temperature	203(2) K	
wavelength	0.710 73 Å	
crystal system	rhombohedral	
space group	$R\bar{3}$	
unit cell dimensions	a = 21.6404(4) Å	$\alpha = 90°$
	b = 21.6404(4) Å	$\beta = 90°$
	c = 53.188(3) Å	$\gamma = 120°$
volume	21 571.1(12) Å^3	
Z	9	
density (calcd)	1.275 Mg/m^3	
absorption coefficient	0.656 mm^{-1}	
F(000)	8523	
crystal size	0.58 × 0.48 × 0.24 mm^3	
θ range for data collection	1.15−25.10°	
index ranges	$-25 \le h \le 25$	
	$-25 \le k \le 25$	
	$-63 \le l \le 63$	
reflections collected	130 040	
independent reflections	8552 [R(int) = 0.0461]	
completeness to θ = 25.10°	99.9%	
absorption correction	semiempirical from equivalents	
max and min transmission	0.854 and 0.717	
refinement method	full-matrix least-squares on F^2	
data/restraints/parameters	8552/2/533	
goodness-of-fit on F^2	1.062	
final R indices [$I > 2\sigma(I)$]	$R1$ = 0.0728, w$R2$ = 0.2299	
R indices (all data)	$R1$ = 0.0804, w$R2$ = 0.2390	
largest diff peak and hole	2.741 and −1.992 e·Å^{-3}	

Single crystals suitable for X-ray diffraction were grown by diffusion of diisopropyl ether into a solution of $[(Cu(PPh_3)_2)_3(HATNMe_6)](BF_4)_3$ in 1,2-dichloroethane. Crystal data, data collection and refinement parameters are listed in Table 1. Measurements were made with a Bruker diffractometer equipped with an Apex II charge-coupled device (CCD) area detector using graphite monochromated Mo Kα (λ = 0.710 73 Å) radiation. The structures were solved by direct methods and refined on F^2 by use of all data in full-matrix least-squares procedures. All non-hydrogen atoms were refined with anisotropic displacement parameters. Hydrogen atoms were included in calculated positions with isotopic displacement parameters 1.2 times the isotropic equivalent of their carrier carbon atoms. One full molecule of 1,2-dichloroethane was included in the structure disordered with its decomposition product 2-chloroethanolwith 50/50 occupancy. All three BF_4 anions appear on 3-fold axes, one between cations and the other two on the same axis, one above and one below the central ring of the cation. While one of these two anions was well-ordered, the other seemed to include some solvent/position disorder. Attempts to model this disorder met with only a small improvement in the quality of the structure and no change to the cation, which is the focus of the investigation. Hence, the disordered anion was restrained to a typical conformation and the residual solvent component was removed by use of the SQUEEZE algorithm. All software was contained in the Apex II software package supplied by Bruker AXS, Madison, WI; or PLATON.[31][A. L. Spek (2007) Utrecht University, Utrecht, The Netherlands]. CCDC 654380 contains the supplementary crystallographic data for this paper. These data can be obtained free of charge from The Cambridge Crystallographic Data Centre via www.ccdc.cam.ac.uk/data_request/cif.

FT-IR spectra of potassium bromide discs of the compounds were obtained on a Perkin-Elmer Spectrum BX FT-IR system with Spectrum v. 2.00 software. Spectra were measured via 64 scans, and band positions are reproducible to 1−2 cm^{-1}.

FT-Raman spectra were collected on powder samples by use of a Bruker IFS-55 interferometer with an FRA/106 S attachment. The excitation source was an Nd:YAG laser with an excitation wavelength of 1064 nm. A Ge diode (D425) operating at room temperature was used to detect Raman photons. All spectra were taken with a laser power of 80 mW at the sample and a resolution of 4 cm^{-1}. Spectra were obtained via 64−256 scans and spectra were analyzed with GRAMS 5.0 (Galactic Industries).

Instrumentation used for the resonance Raman experiments has been described elsewhere.[18,21,32−36] Briefly, a continuous-wave krypton-ion laser (Innova I-302, Coherent, Inc.), solid-state 444 nm diode (Crystal Laser), solid-state 532 nm Nd:YAG (B&W Tec Inc.), helium−neon (Oplectra, Germany) or argon-ion lasers (Melles Griot Omnichrome MAP-543) were used to generate resonance Raman scattering. Band-pass filters removed the ion plasma emission lines from the laser output. The laser output was adjusted to give between 5 and 10 mW at the sample. The incident beam and the collection lens were arranged in a 135° back-scattering geometry to reduce Raman intensity reduction by self-absorption.[18] An aperture-matched lens was used to focus scattered light through a narrow-band line-rejection (notch) filter (Kaiser Optical Systems) and a quartz wedge (Spex) and onto the 100 μm entrance slit of a spectrograph (Acton Research SpectraPro 500i). The collected light was dispersed in the horizontal plane by a 1200 grooves/mm ruled diffraction grating (blaze wavelength 500 nm) and detected by a liquid nitrogen-cooled back-illuminated Spec-10:100B CCD controlled by a ST-133 controller and WinSpec/32 (version 2.5.8.1) software (Roper Scientific, Princeton Instruments).

Wavenumber calibration was performed with Raman bands from a 1:1 (by volume) mixture of acetonitrile and toluene.[37] Peak positions were reproducible to within 1 cm^{-1}. Calibration spectra were obtained with a resolution of 3−5 cm^{-1}. Peak positions were reproducible to within 1−2 cm^{-1}. Sample spectra were obtained with a resolution of 5 cm^{-1}. Freshly prepared samples were held in a spinning NMR tube. The concentration of the solute was approximately 5 mmol L^{-1}. Spectral intensities were corrected for self-absorption,[38] differential band pass and throughput of the spectrograph, and detector sensitivity. Integrated band intensities were obtained from the peak-fitting module in Origin Pro 7.5 (Origin Laboratory). Solute differential Raman cross-sections, $d\sigma_R/d\Omega$, were obtained relative to solvent cross-sections by use of the equation

$$\left(\frac{d\sigma_R}{d\Omega}\right)_u = \frac{I_u}{I_v}\frac{c_v}{c_u}\left(\frac{d\sigma_R}{d\Omega}\right)_v \quad (1)$$

where u and v refer to the solute and solvent, respectively. I is the intensity of the peak and c is the concentration. In these experiments the standard used was chloroform.[39] Resonance Raman spectra were obtained with excitation wavelengths of 406, 413.1, 444.0, 457.9, 488.0, 514.5, 532.0, 568, and 647 nm.

Electronic absorption spectra were recorded on a Varian Cary 500 scan UV−vis−near-IR spectrophotometer, with Cary WinUV software. Samples were typically ~10^{-4} mol L^{-1}.

In vacuo geometry optimizations and calculation of harmonic vibrational frequencies were performed by density functional theory (DFT), employing the B3LYP functional.[40,41] In vacuo time-dependent density functional theory (TD-DFT) calculations were carried out with the BLYP functional, as calculated results with the B3LYP functional were not physically reasonable (vide infra). All of these calculations employed the 6-31G(d) basis set within D_{3h} symmetry and were implemented with the Gaussian 03W program package[42] (versions B04 and C02). To simplify the calculation, the PPh_3 groups of the actual complex were supplemented with PH_3 units during the calculation. This has been found previously to be an acceptable simplification in such systems[22,43] The Raman intensities were calculated for the Raman activity at 1064 nm excitation.[44−46] Calculated vibrational wavenumbers were scaled by 0.975, a factor that we have found suitable for metal−polypyridyl complexes.[22,36,43,47−49] The visualization of vibrational modes was provided by the Molden package[50] and GaussViewW (Gaussian Inc.).

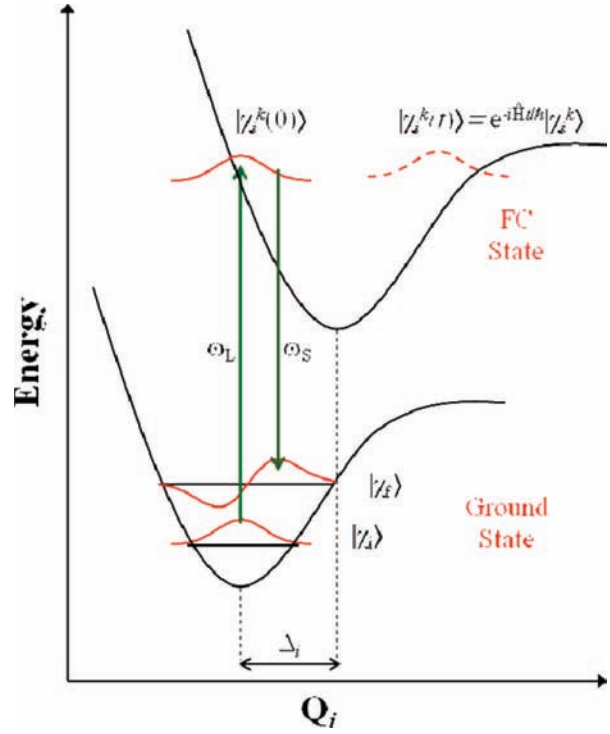

Figure 3. Time-domain picture of molecular spectroscopy. Wavepacket dynamics on the excited-state surface determine a time-dependent overlap integral with the ground-state wave functions. For absorption, the overlap integral involves the ground-state $n = 0$ vibration.

Wavepacket Modeling. The resonance Raman intensities were modeled by use of the time-dependent wavepacket theory first developed by Heller et al.[6,51−53] In this, the excited surface is modeled semiempirically (details below) and it is convenient to use a dimensionless displacement value, Δ_i, which quantifies the structural distortion between the ground and electronically excited multidimensional potential surfaces along the ith vibrational mode. Absorption spectra and resonance Raman data were modeled simultaneously with the same material parameters to provide a check on the quality of the fit to the experimental Raman data.

A brief discussion of the theory behind resonance Raman excitation profiles (RREP) modeling is presented herein. For more detailed discussions the reader is referred to articles by Myers et al.[38,54] The resonant Raman amplitudes are modeled by use of the semiempirical formalism developed by Heller et al.[6,51−53]

The Raman amplitude between the initial and final vibrational states, α_{ij}, is calculated as the half-Fourier transform of the time-dependent overlap of a wavepacket propagating on the kth resonant electronic excited and the $v'' = 1$ ground-electronic-state vibrational wave function by use of eq 2(see Figure 3):

$$\alpha_{ij}^{k}(\omega_L, \delta) = \frac{|\mu_{k0}|^2}{\hbar} \int_0^\infty dt \, \langle \chi_f | \chi_i^k(t) \rangle \times \exp[i(\omega_L - \omega - \delta + \omega_i)t - g(t)] \quad (2)$$

where ω_L is the incident laser frequency, $\hbar\omega_i$ is the energy of the initial vibrational level (set to zero as scattering from all modes in the simulation occurs from the ground vibrational level), ω is the zero−zero electronic transition frequency, and δ is the electronic zero−zero frequency shift due to inhomogeneous broadening. $\langle \chi_f | = \langle f | \mu_0$ and $\langle \chi_i | = \langle i | \mu_0$ are the multidimensional ground-state vibrational wave functions multiplied by the transition dipole moment, and $|\chi_i(t)\rangle = \exp(-iHt/\hbar)|\chi_i\rangle$ is the initial vibrational wave function propagated for a time, t, on the electronic excited-state surface, by the excited-state vibrational Hamiltonian. $g(t)$ is the solvent broadening function modeled as an overdamped Brownian oscillator.[55] Separable harmonic oscillators, with frequencies taken from the ground-state Raman modes, were used in the model for the potential energy surfaces. Ground- and excited-state normal modes are assumed to have the same form—that is, Dushinsky rotation is neglected—and non-Condon effects are also neglected.

The experimental observable, the differential Raman cross-section, is calculated via eq 3:

$$\left(\frac{d\sigma}{d\Omega}\right)_{\parallel+\perp} = \sum_i B_i \sum_f \int d\omega_S \times \left(\frac{\omega_S{}^3 \omega_L}{c^4} \int_{-\infty}^{+\infty} d\delta \, G(\delta) |\alpha_k(\omega_L, \delta)|^2 \right) L_{if}(\omega_L - \omega_S) \quad (3)$$

where B_i is the Boltzmann population of the initial vibrational state (assumed to be unity here) and $L_{if}(\omega_L - \omega_S)$ is a Raman line-shape function. $G(\delta)$ is a normalized inhomogeneous broadening function which is taken to be Gaussian.

The absorption cross-section is calculated at the same level of theory via eq 4:

$$\sigma_A(\omega) = \frac{4\pi|\mu|^2\omega}{3n\hbar c} \sum_i B_i \int_{-\infty}^{+\infty} d\delta \, G(\delta) Re \int_{-\infty}^{+\infty} dt \, \langle \chi_i | \chi_i(t) \rangle \exp[i(\omega_L - \omega - \delta + \omega_i)t - g(t)] \quad (4)$$

where the real part of the Fourier transform is taken and n is the refractive index of the solvent.

In the case of two resonant electronic states, the Raman amplitude is calculated for each excited-state surface and then summed before the modulus square is taken to obtain the Raman intensity. The absorption cross-section is a simple sum of the two electronic transitions. The angle between the transition dipole moments of the electronic transitions was taken to be zero on the basis of DFT calculations (vida infra). It is possible for vibrational modes to have displacements of opposite signs in each electronic state, although only the relative sign carries any significance.

The fits are insensitive to the value of the inhomogeneous broadening parameter. We use an initial value of 0.0 cm^{-1} for the inhomogeneous broadening, even though some inhomogeneous broadening is likely to be occurring.

III. Results and Discussion

a. Experimental and Calculated Structure of $[(Cu(PPh_3)_2)_3(HATNMe_6)]^{3+}$. Crystallographic data for the solvated trinuclear complex $[(Cu(PPh_3)_2)_3(HATNMe_6)](BF_4)_3$ are presented in Table 1, and a depiction of the structure of the complex cation is shown in Figure 4. Compared to the free ligand,[56] the bond lengths within the complex show little variation. C−C bond lengths in the central benzene ring shrink slightly from of 1.425 and 1.479 Å for the free ligand to 1.416 and 1.455 Å for the copper complex. Neither the fused ring C−C bonds nor the C−N bonds of the diimine chelate ring change significantly in length upon coordination of the Cu(I) ions. There is a small but significant twisting of the entire aromatic $HATNMe_6$ unit in the complex; the mean planes of the central ring and the pyrazine rings are at angles from 0.85° to 1.03° to each other in the free ligand and this increases to 3.90° in $[(Cu(PPh_3)_2)_3(HATNMe_6)]^{3+}$. Similarly, the mean plane angles between the central and outer rings are between 1.60° and 1.68° in the free ligand and 6.93° in $[(Cu(PPh_3)_2)_3(HATNMe_6)]^{3+}$. Such distortions have been seen in the few other crystallographically characterized examples of complexes containing three metal ions coordinated to the $HATNMe_6$ ligand: in $[(TiCp_2)_3HATNMe_6]$[57] and polymeric trisilver complexes of $HATNMe_6$,[58,59] mean plane angles between the central and pyrazine rings range from 1.07° to 6.15°, while those between the central and outer rings vary between 1.82° and 11.34°. This distortion of the ligand is also manifested in the N−C−C−N torsion angle within the chelate rings. In the $[(Cu(PPh_3)_2)_3(HATNMe_6)]^{3+}$ cation, this angle is 5.38°, similar to that observed in both $[Cu(phen)(PPh_3)_2]NO_3$ (3.62°)[60] and $[Cu(phen)(PPh_3)_2]NO_3 \cdot 1.5EtOH$ (6.15°).[61] The Cu−N (2.113 and 2.135 Å) and Cu−P (2.271 and 2.284 Å) bond lengths in the $[(Cu(PPh_3)_2)_3(HATNMe_6)]^{3+}$ cation are also similar to those in $[Cu(phen)(PPh_3)_2]NO_3$ (Cu−N, 2.084 and 2.104 Å; Cu−P, 2.285 and 2.258 Å) and $[Cu(phen)(PPh_3)_2]NO_3 \cdot 1.5EtOH$ (Cu−N, 2.081 and 2.070 Å; Cu−P, 2.245 and 2.271 Å).[60,61]

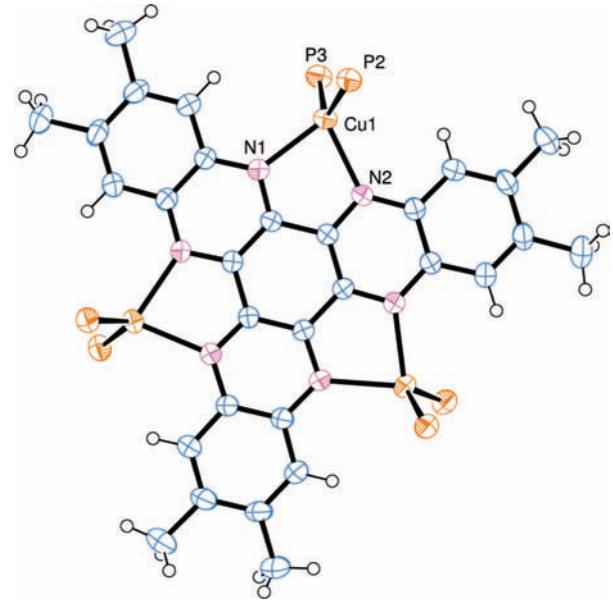

Figure 4. View of the $[(Cu(PPh_3)_2)_3(HATNMe_6)]^{3+}$ cation. The phenyl rings of the PPh_3 ligands have been removed for clarity. Selected bond lengths (in angstroms): Cu(1)−N(1) 2.113(3); Cu(1)−N(2) 2.135(3); Cu(1)−P(2) 2.2710(11); Cu(1)−P(3) 2.2837(11). Selected bond angles (in degrees): N(1)−Cu(1)−N(2) 78.98(11); N(1)−Cu(1)−P(2) 113.74(9); N(2)−Cu(1)−P(2) 106.79(9); N(1)−Cu(1)−P(3) 106.43(9); N(2)−Cu(1)−P(3) 115.59(9); P(2)−Cu(1)−P(3) 125.77(4).

There is satisfactory agreement between the optimized structure parameters of $[(Cu(PH_3)_2)_3(HATNMe_6)]^{3+}$ and the crystallographic data for $[Cu(PPh_3)_3(HATNMe_6)]^{3+}$. Bond length variation between the experimental and calculated data has a

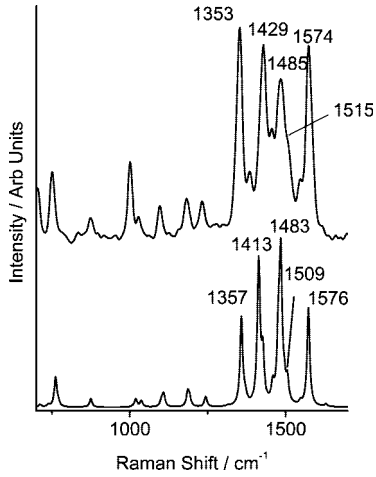

Figure 5. (Upper trace) Normal Raman spectrum (λ_{exc} = 1064 nm, 100 mW, 10 min acquisition) of the solid-state sample of $[(Cu(PPh_3)_2)_3(HATNMe_6)](BF_4)_3$. (Lower trace) Calculated Raman spectrum of $[(Cu(PH_3)_2)_3(HATNMe_6)]^{3+}$.

mean average deviation of <0.01 Å for the ligand and 0.08 Å for the metal nitrogen linkages.

b. Experimental and Calculated Raman Spectra $[(Cu(PPh_3)_2)_3(HATNMe_6)]^{3+}$. Frequency calculations on the optimized structure revealed no negative vibrational frequencies, indicating that the optimized structure is at an energy minimum. Furthermore, the observed and calculated Raman spectra correlate well, with a mean absolute deviation of 8 cm^{-1} for the 1000−1600 cm^{-1} region and with qualitative intensity agreement. That is, the strongest experimentally observed bands at 1574, 1485, 1429, and 1353 cm^{-1} are predicted to be intense bands at 1576, 1483, 1413, and 1357 cm^{-1}, respectively (Figure 5). The good level of agreement between predicted and experimental vibrational spectra provides some level of confidence in the other calculated parameters.

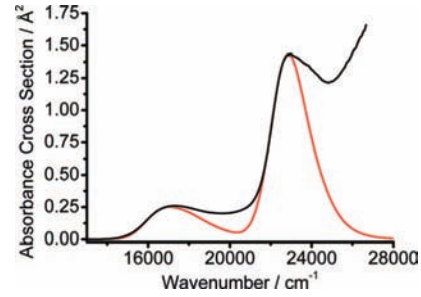

Figure 7. Electron absorption spectrum of $[(Cu(PPh_3)_2)_3(HATNMe_6)]^{3+}$ (black line) and simulated absorption spectrum (red line) from calculated spectroscopic parameters (see Table 3).

A selection of the normal modes is depicted in Figure 6. These reveal that some of the vibrations, notably $\nu(174)$, result in a very significant perturbation of the central ring, which compresses while the other pyrazine rings expand, and vice versa. Some of the other normal modes [$\nu(93)$, $\nu(205)$, and $\nu(212)$] have only small central and pyrazine ring contributions and consist predominantly of outer-ring vibrations.

c. Electronic Spectra. The electronic absorption spectrum of $[(Cu(PPh_3)_2)_3(HATNMe_6)]^{3+}$ in $CHCl_3$ and the simulated fit from wavepacket analysis are shown in Figure 7. The experimental spectrum shows two broad absorptions in the visible region lying at 17 000 cm^{-1} (590 nm) and 23 000 cm^{-1} (430 nm). The spectrum of the free ligand shows a strong transition at 410 nm attributed to the LC transition of the HATN ring system.[30] A number of related complexes have been reported in the literature. The Ag(I) coordination polymer forms as orange crystals;[62] the $Re(CO)_3Cl$ complex with $HATNMe_6$ lies at 514 nm and is assigned as an MLCT transition; and the corresponding $PdCl_2$ complex has an absorption at 466 nm.[63] TD-DFT analyses of the free ligand suggest this band is entirely highest occupied to lowest unoccupied molecular orbital (HOMO to LUMO) in nature. The slight red shift in the higher energy

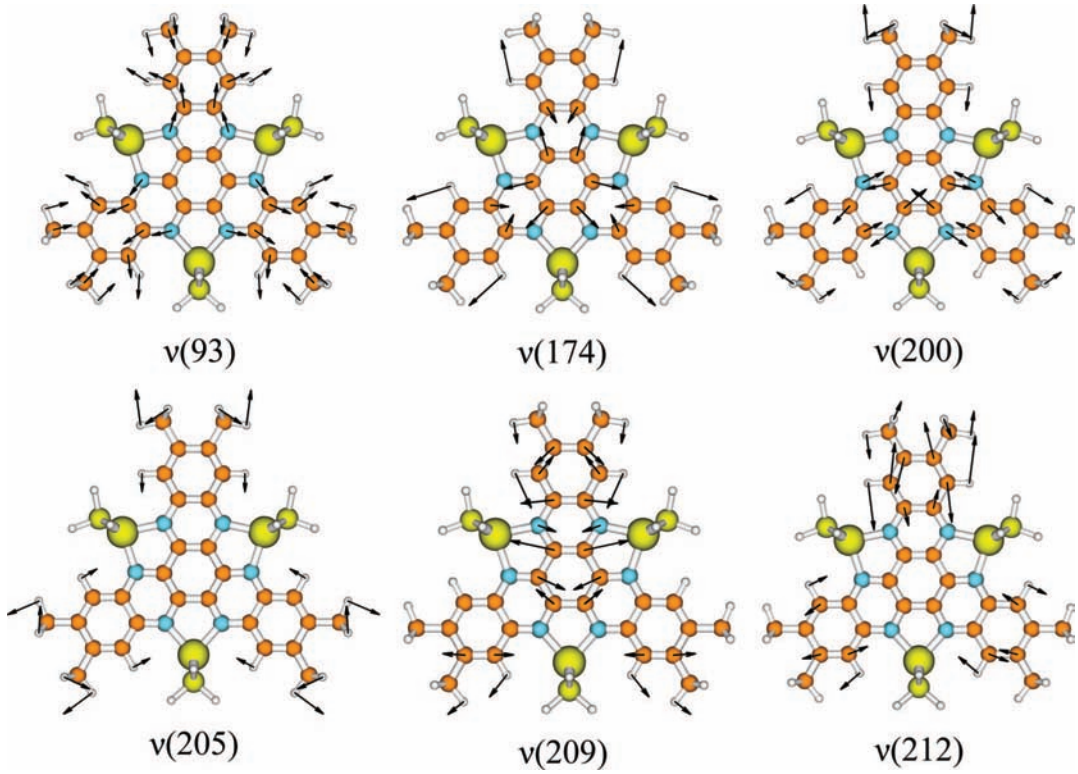

Figure 6. Eigenvectors for selected calculated normal modes of vibration of $[(Cu(PH_3)_2)_3(HATNMe_6)]^{3+}$.

TABLE 2: Experimental Electronic and TD-DFT Data on $[(Cu(PPh_3)_2)_3(HATNMe_6)]^{3+}$

experimental			calculated			
λ, nm	ε, 10^3 M^{-1} cm^{-1}	ν, 10^3 cm^{-1}	λ, nm	f	assignment	MO configuration, major components
590	4.1	18.1	641	0.08	MLCT	HOMO − 4, HOMO − 3, LUMO + 1, LUMO + 2
		20	540	0.08	MLCT	HOMO − 13, HOMO − 12, LUMO
430	22	21.6	500	0.11	LC	HOMO − 11, HOMO − 11, LUMO

TABLE 3: Parameters from Wavepacket Simulation of $[(Cu(PPh_3)_2)_3(HATNMe_6)]^{3+}$

	frequency (cm^{-1})		band I (low energy)		band II (high energy)	
mode	exptl	calcd	Δ	λ_v (cm^{-1})	Δ	λ_v (cm^{-1})
212	1630	1628	0.24	46.9	0.11	9.9
210	1574	1570	0.18	25.5	0.14	15.4
209	1550	1545	0.29	65.2	0.12	11.2
208	1515	1504	0.52	204.8	0.28	59.4
205	1494	1493	0.28	58.6	0.17	21.6
200	1485	1482	0.39	112.9	0.21	32.7
186	1429	1424	0.1	7.1	0.2	28.6
177	1368	1400	0.2	27.4	0.15	15.4
174	1353	1355	0.4	108.2	0.2	27.1
172	1313	1313	0.2	26.3	0.05	1.6
165	1247	1242	0.14	12.2	0.13	10.5
160	1182	1183	0.18	19.1	0.19	21.3
154	1125	1107	0.2	22.5	0.07	2.8
152	1108	1105	0.2	22.2	0.06	2.0
123	845	873	0.4	67.6	0.15	9.5
110	707	737	0.15	8.0	0.15	8.0
101	647	654	0.3	29.1	0.15	7.3
93	592	590	0.75	166.5	0.2	11.8
vibrational reorg energy, cm^{-1}					1030.2	296.0
total vibrational reorg energy, cm^{-1}						**1326.2**
electronic origin (E_{oo}), cm^{-1}					15 100	21 300
homogenous broadening (Γ_o), cm^{-1}					1790	1860
electronic dipole length (μ), Å					0.86	1.52
classical reorg energy (λ_s), cm^{-1}					1450.3	1566
total classical reorg energy (λ_s), cm^{-1}						**3016.3**

transition observed in the complex may suggest additional electronic character in this transition previously unavailable to the free ligand. The electronic transitions of the complex are modeled by use of time-dependent density functional theory (TD-DFT) at the BLYP/6-31G(d) level. These data, with the experimental measurements, are summarized in Table 2. In these calculations two MLCT transitions are predicted: the lowest energy MLCT transition is calculated at 641 nm and primarily consists of HOMO − 3, HOMO − 4 → LUMO + 1, LUMO + 2 excitations. The higher energy MLCT transition of similar intensity is calculated at 540 nm and comprises HOMO − 12, HOMO − 13 → LUMO excitations. A transition considered ligand-centered (LC) in character is calculated at 500 nm and involves population of the LUMO and degenerate LUMO + 1, LUMO + 2 orbital sets from numerous occupied π orbitals. The calculated energies and intensities are in reasonable agreement with experiment, and importantly, the calculated orbital contributions to the transitions make physical sense with respect to the photophysics of metal polypyridyl complexes.

Calculations of the same system invoking the B3LYP/6-31G(d) TD-DFT method do not give physically reasonable results. Two MLCT transitions and one LC transition of energies comparable to experiment are calculated. However the oscillator strength predicted for the higher energy MLCT transition (HOMO, HOMO − 1 → LUMO + 1) is far too intense (f = 0.3), which corresponds to an extinction coefficient of 47 000 M^{-1} cm^{-1}. This is much too high and rather unrealistic in comparison to the experimental data. The uncertainties present in B3LYP/6-31G(d) TD-DFT calculations mean such results are often reported to be significantly offset in terms of energy and modestly reliable in terms of oscillator strengths.[64−66] The breakdown of TD-DFT in prediction of transition energies for charge-transfer states has been the subject of a number of papers.[64−66] Notably, Dreuw and Head-Gordon[65] have shown that the reason for the very poor modeling of methods such as B3LYP lies in the fact that the approximate exchange correlations used in such methods propagate errors and do not behave correctly with respect to distance (R) between the charge-transfer donor and acceptor ($1/R$). Thus for MLCT transitions one might at best expect qualitative agreement between calculations and experiment depending on how much charge-transfer nature exists in the transition.

d. Resonance Raman Spectra and Wavepacket Modeling. The electronic absorption spectrum of $[(Cu(PPh_3)_2)_3(HATNMe_6)]^{3+}$ is dominated by two bands and these are probed by measuring resonance Raman spectra at wavelengths across the two experimentally observed transitions. In the resonance Raman spectrum with excitation at 444 nm, many bands are observed, some of which are very weak in the nonresonant spectrum; these are shown in Figure 9 along with the mode labels from the calculated frequency data. The notable Raman bands [associated modes in brackets] in the nonresonant spectrum (Figure 5) lie at 1353 [ν(174)], 1429 [ν(196)], 1485 [ν(200)], and 1574 [ν(209)] cm^{-1}, while the spectrum with 444 nm excitation (Figure 9) shows additional features at 592 [ν(93)], 1182 [ν(160)], 1515 [ν(205)], and 1630 [ν(212)] cm^{-1}. As the excitation wavelength is tuned to the red, differing relative intensity patterns emerge. The resonance Raman spectra of the complex going across the excitation wavelengths are shown in Figure 10. By measurement of the corrected Raman intensities, it is possible to derive the Raman cross sections for each band as a function of excitation wavelength. The Raman cross sections fall significantly upon going to red excitation (Figure 11) and the relative band intensity patterns approach those of the nonresonant spectrum.

The wavepacket analyses for the complex yields two electronic transitions, labeled band I and band II (Table 3). These two transitions provide a good match to the observed electronic absorption spectrum (Figure 7) and very satisfactory fitting to the resonance Raman excitation profiles (Figure 11). Inspection of the individual Δ values for each mode reveal that some have much greater displacements in the low-energy than high-energy transition, notably ν(93), ν(174), ν(200), and ν(205). One may rationalize this result through consideration of the DFT frequency and TD-DFT calculations. From the TD-DFT calculation it is evident that the dominant acceptor MO in one of the MLCT transitions is the LUMO. The LUMO has a very distinctive bonding/antibonding shape in which the central ring is strongly bonded with the three attached pyrazine rings being antibonded with population of the orbital. If one examines the normal modes, it is clear that ν(174) strongly mimics the bonding changes that will occur with population of the LUMO. It compresses the central ring while stretching the pyrazines. Additionally, there are many modes that will to some degree reflect these structural changes resulting from LUMO population. However, the difference in enhancement patterns and thus

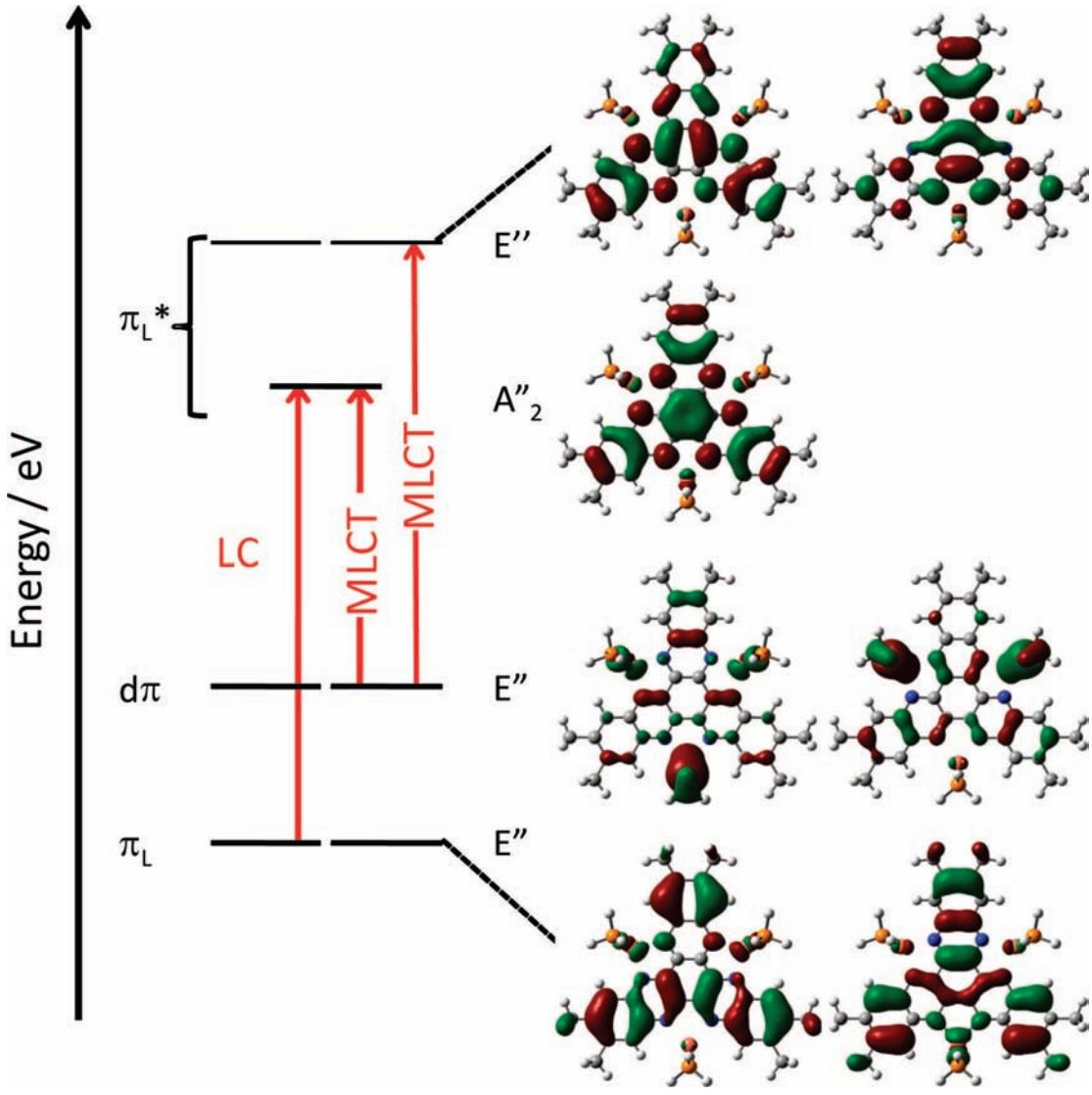

Figure 8. Energy levels and selected molecular orbital pictures: LUMO + 2, LUMO +1 π_L*(E″); LUMO π_L*(A_2″); HOMO, HOMO − 1 dπ; HOMO − 10, HOMO − 11 π_L for $[(Cu(PH_3)_2)_3(HATNMe_6)]^{3+}$.

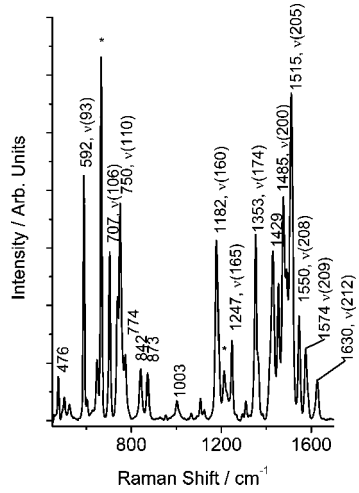

Figure 9. Resonance Raman spectrum of $[(Cu(PPh_3)_2)_3(HATNMe_6)]^{3+}$ with 444 nm excitation; selected wavenumbers and corresponding calculated mode labels are given. *Solvent bands.

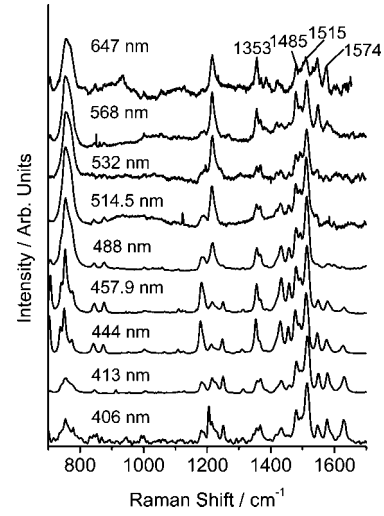

Figure 10. Resonance Raman spectra of $[(Cu(PPh_3)_2)_3(HATNMe_6)]^{3+}$ (solvent, laser power, acquisition time) at differing excitation wavelengths.

the subsequent calculated Δ values need not, and should not, be attributed solely to the nature of the acceptor orbital but also the donor MOs. The TD-DFT calculations predict the presence of two MLCT-type transitions at 641 and 540 nm. These are dπ → π* (LUMO) and dπ → π* (LUMO + 1, LUMO + 2) in

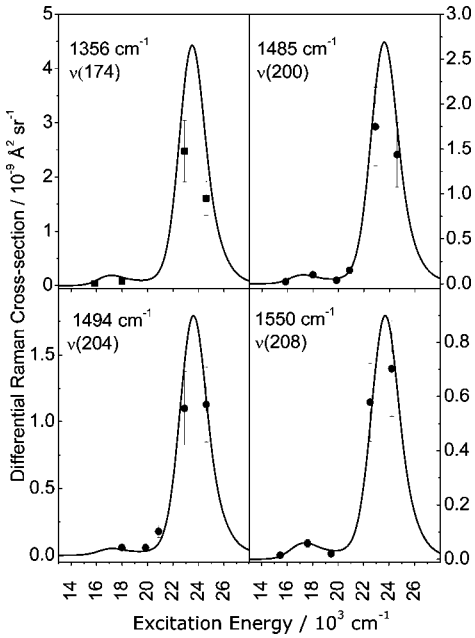

Figure 11. Resonance Raman excitation profiles for some of the vibrations observed in the spectra of $[(Cu(PPh_3)_2)_3(HATNMe_6)]^{3+}$.

character. A higher energy transition is predicted at 500 nm that involves a pair of MOs (HOMO − 11 and HOMO − 10) as donor orbitals. These π orbitals, HOMO − 11 and HOMO − 10, have considerable bonding and antibonding character across all three types of rings in HATN, namely the central, pyrazine, and outer rings. Importantly, neither of these MOs has the distinctive bonding/antibonding nature for the central and pyrazine rings, respectively. Judging by the nature of these MOs, it is unsurprising that many HATN modes are enhanced by this type of transition. However, the LUMO, HOMO − 10, and HOMO − 11 are all, broadly speaking, bonding in nature with respect to the outer rings. Thus excitation from HOMO − 10, or HOMO − 11, to the LUMO will induce little structural distortion of the ligand in the outer ring section. The calculated Δ values for specific normal modes are consistent with this picture. For $\nu(93)$ the mode is almost exclusively outer-ring character, and $\nu(205)$ has significant outer-ring motion with additional other ring contributions. Thus the lower energy transition that originates from dπ orbitals to the LUMO will favor the enhancement of the modes that either stretch and compress the central and pyrazine rings, as does $\nu(174)$, and favor modes that have motion in the outer rings, which change structure with population of the LUMO, LUMO + 1, or LUMO + 2. However, in the higher energy transition the donor and acceptor orbitals are both bonding with respect to the outer rings so that the enhancement of modes which have outer-ring character is diminished, as we observe.

One might argue that it would be more appropriate to model the observed $[(Cu(PPh_3)_2)_3(HATNMe_6)]^{3+}$ absorption spectrum and resonance excitation profiles with three transitions; two of MLCT character and one of LC character. In considering this, one has to appreciate that the wavepacket simulation has a number of varying parameters, and although adding another transition is possible, the data do not warrant such added complexity. The TD-DFT calculations give a good representation of the observed electronic spectrum, and although simple symmetry considerations argue for two MLCT transitions, it appears that our resonance Raman excitation profiles are of insufficient sensitivity to detect a second MLCT transition of appreciable intensity. We have thus taken the pragmatic approach of modeling with two transitions.

The electronic transitions differ quite significantly in their structural parameters: for the lower energy transition (band I), the vibrational reorganization energy (λ_v) is 1030 cm^{-1} and the dipole length is 0.9 Å; and for the higher energy band (band II), $\lambda_v = 300$ cm^{-1} and the dipole length is 1.5 Å. It is instructive to examine the electronic parameters derived from the wavepacket modeling with respect to other studied systems.

The lower energy transition is MLCT in origin and this type of analysis has been performed on a number of metal polypyridyl complexes,[18,19,34,47] including perhaps the most widely studied, namely, $[Fe(bpy)_3]^{2+}$[67] and $[Ru(bpy)_3]^{2+}$;[68] the lowest lying MLCT transitions for both compounds yield λ_v of approximately 1340 cm^{-1}.[69] The bpy unit is a small ligand that undergoes reasonable structural distortion when reduced, as evidenced by the vibrational energy shifts in its ligand skeletal modes.[70] However, Δ analysis for systems in which the ligand is a larger, more delocalized system yields lower values. Howell et al.[34] examined $[Ru(CN)_4(ppb)]^{2-}$, where ppb = dipyrido[2,3-*a*:3′,2′-*c*]phenazine; the lowest energy MLCT transition gave λ_v of 600 cm^{-1}. This is consistent with the photophysical data of Ru(II)ppb complexes, which show long-lived excited states despite having low energies; such behavior is attributed to low k_{nr} values that result from small displacements between the ground and excited states.[48,71] The $[(Cu(PPh_3)_2)_3(HATNMe_6)]^{3+}$ cation falls into this second category: it has a λ_v of 1030 cm^{-1} for the MLCT transition, which is higher than that observed for $[Ru(CN)_4(ppb)]^{2-}$. However, this does not necessarily imply greater ligand distortion on the part of HATN over ppb. The second aspect that must be considered is the role of the metal. In the case of the $[Ru(CN)_4]^{2-}$ moiety, there is reasonable back-bonding between the metal and ligand in the ground state; thus the MLCT transition does not transfer as much electron density as in the case of a $[Cu(PPh_3)_2]^+$ moiety. Consistent with this, the transition dipole length for the $[(Cu(PPh_3)_2)_3(HATNMe_6)]^{3+}$ MLCT transition is 0.9 Å, while that of $[Ru(CN)_4(ppb)]^{2-}$ is 0.6 Å. Finally some care must be taken in examining copper(I) complexes because of the possibility that the probed upper surface may contain torsional motion and an expansion of the coordination sphere from 4 to 5, which can occur in MLCT excitation of such compounds.[61,72−74] Recently, wavepacket modeling with resonance excitation profiles was used to probe the MLCT transitions of $[Cu(L)_2]^+$, where L = bpy, phen, dmp.[20] The studies of these complexes are complicated by the fact that each has two close-lying MLCT transitions of differing orbital parentage. Nonetheless, for the lowest energy transition, λ_v is 2000 cm^{-1} for $[Cu(bpy)_2]^+$ and less than 1000 cm^{-1} for the other compounds. This is consistent with the fact that phen and dmp are known to undergo very small structural changes upon reduction, as evidenced by the minimal shifts in the ligand modes upon reduction.[22] Further to this, the outer-sphere reorganization (λ_s) is 4000 cm^{-1} for $[Cu(bpy)_2]^+$ and $[Cu(phen)_2]^+$ and only 2500 cm^{-1} for $[Cu(dmp)_2]^+$. For $[(Cu(PPh_3)_2)_3(HATNMe_6)]^{3+}$, λ_s is 1800 cm^{-1}, which is reasonable considering the steric bulkiness of the PPh_3 units, which does not favor expansion of the coordination sphere.

Conclusions

In this study we have synthesized and structurally characterized a trinuclear copper(I) complex with the tribridging ligand $HATNMe_6$. We have examined the electronic structure of this compound using density functional theory calculations and resonance Raman spectroscopy. We find the following: (1) The

X-ray structure of solvated $[(Cu(PPh_3)_2)_3(HATNMe_6)](BF_4)_3$ shows that the $HATNMe_6$ ligand is slightly twisted, with a mean plane angle between the central and outer rings of 6.93°, as has been seen in other structurally characterized Ti_3 and Ag_3 complexes of the $HATNMe_6$ ligand. (2) Calculations on the complex show good agreement with experimental data in terms of structure and vibrational spectra. (3) The electronic spectrum of the complexes shows two bands in the visible region attributed to ligand-centered and metal-to-ligand charge-transfer, respectively. Time-dependent DFT calculations show good agreement with experiment, with two MLCT and one LC transition predicted in the visible region (641, 540, and 500 nm). (4) Resonance Raman spectra of the complex using excitation energy across the range 647−406 nm at a series of discrete wavelengths were measured and these showed a variation in enhancement patterns consistent with two distinct transitions. (5) The absolute Raman cross sections are evaluated and, through a wavepacket analysis, structural and electronic properties for the transitions are established. This may be done by considering two transitions, one of which is MLCT in nature, with substantial Δ values, and the other LC in nature with lower Δ values. The pattern of Δ values shows good agreement with the observed calculated modes. For example, the MLCT transition shows much larger Δ values for outer-ring modes such as $\nu(93)$ and $\nu(205)$ than in the LC transition. The behavior of these states may be rationalized by considering the MOs and the TD-DFT calculations in which the donor orbitals for the LC transition have similar outer-ring bonding characteristics compared to the MLCT transition, which has no donor orbital bonding characteristics on the ligand because the donor MOs are dπ orbitals.

These data reveal that it is possible to understand the electronic nature of these types of complexes: importantly, they reveal that the ligand localizes negative charge on its LUMO, LUMO + 1, and LUMO + 2 orbitals with both MLCT and LC excitation. It is hoped that liquid crystalline systems will be obtained from these types of compounds.

Acknowledgment. The support of the Foundation of Research Science and Technology, the Royal Society of New Zealand (Marsden Fund), and the MacDiarmid Institute for Advanced Materials and Nanotechnology is gratefully acknowledged.

References and Notes

(1) Ong, C. W.; Liao, S.-C.; Chang, T. H.; Hsu, H.-F. *Tetrahedron Lett.* **2003**, *44*, 1477.
(2) Crispin, X.; Cornil, J.; Friedlein, R.; Okudaira, K. K.; Lemaur, V.; Crispin, A.; Kestemont, G.; Lehmann, M.; Fahlman, M.; Lazzaroni, R.; Geerts, Y.; Wendin, G.; Ueno, N.; Bredas, J.-L.; Salaneck, W. R. *J. Am. Chem. Soc.* **2004**, *126*, 11889.
(3) Clark, R. J. H.; Dines, T. J. *Angew. Chem.* **1986**, *98*, 131.
(4) Hirakawa, A. Y.; Tsuboi, M. *Science* **1975**, *188*, 359.
(5) Myers, A. B. *J. Raman Spectrosc.* **1997**, *28*, 389.
(6) Heller, E. J. *Acc. Chem. Res.* **1981**, *14*, 368.
(7) Hung, S. T.; Wang, C. H.; Kelley, A. M. *J. Chem. Phys.* **2005**, 123.
(8) Lilichenko, M.; Kelley, A. M. *J. Chem. Phys.* **1999**, *111*, 2345.
(9) Lilichenko, M.; Tittelbach-Helmrich, D.; Verhoeven, J. W.; Gould, I. R.; Myers, A. B. *J. Chem. Phys.* **1998**, *109*, 10958.
(10) Kulinowski, K.; Gould, I. R.; Ferris, N. S.; Myers, A. B. *J. Phys. Chem.* **1995**, *99*, 17715.
(11) Kulinowski, K.; Gould, I. R.; Myers, A. B. *J. Phys. Chem.* **1995**, *99*, 9017.
(12) Markel, F.; Ferris, N. S.; Gould, I. R.; Myers, A. B. *J. Am. Chem. Soc.* **1992**, *114*, 6208.
(13) Myers, A. B. *Chem. Phys.* **1994**, *180*, 215.
(14) Myers, A. B. *Chem. Rev.* **1996**, *96*, 911.
(15) Phillips, D. L.; Gould, I. R.; Verhoeven, J. W.; Tittelbach-Helmrich, D.; Myers, A. B. *Chem. Phys. Lett.* **1996**, *258*, 87.
(16) Moran, A. M.; Delbecque, C.; Kelley, A. M. *J. Phys. Chem. A* **2001**, *105*, 10208.
(17) Moran, A. M.; Kelley, A. M. *J. Chem. Phys.* **2001**, *115*, 912.
(18) Waterland, M. R.; Howell, S. L.; Gordon, K. C.; Burrell, A. K. *J. Phys. Chem. A* **2005**, *109*, 8826.
(19) Howell, S. L.; Gordon, K. C. *J. Phys. Chem. A* **2006**, *110*, 4880.
(20) Lind, S. J.; Gordon, K. C.; Waterland, M. R. *J. Raman Spectrosc.* **2008**, *39*, 1556.
(21) Lundin, N. J.; Walsh, P. J.; Howell, S. L.; McGarvey, J. J.; Blackman, A. G.; Gordon, K. C. *Inorg. Chem.* **2005**, *44*, 3551.
(22) Howell, S. L.; Gordon, K. C. *J. Phys. Chem. A* **2004**, *108*, 2536.
(23) Clarke, T. M.; Gordon, K. C.; Officer, D. L.; Hall, S. B.; Collis, G. E.; Burrell, A. K. *J. Phys. Chem. A* **2003**, *107*, 11505.
(24) Earles, J. C.; Gordon, K. C.; Officer, D. L.; Wagner, P. *J. Phys. Chem. A* **2007**, *111*, 7171.
(25) Diaz-Acosta, I.; Baker, J.; Cordes, W.; Pulay, P. *J. Phys. Chem. A* **2001**, *105*, 238.
(26) Dattelbaum, D. M.; Omberg, K. M.; Schoonover, J. R.; Martin, R. L.; Meyer, T. J. *Inorg. Chem.* **2002**, *41*, 6071.
(27) Dattelbaum, D. M.; Martin, R. L.; Schoonover, J. R.; Meyer, T. J. *J. Phys. Chem. A* **2004**, *108*, 3518.
(28) Dattelbaum, D. M.; Omberg, K. M.; Hay, P. J.; Gebhart, N. L.; Martin, R. L.; Schoonover, J. R.; Meyer, T. J. *J. Phys. Chem. A* **2004**, *108*, 3527.
(29) Farrell, I. R.; van Slageren, J.; Zalis, S.; Vlcek, A. *Inorg. Chim. Acta* **2001**, *315*, 44.
(30) Gordon, K. C.; David, G.; Walsh, T. J. *Spectrochim. Acta, Part A* **2009**, *72*, 209.
(31) Spek, A. L. *Acta Crystallogr., Sect. A* **1990**, *A46*, 34.
(32) Walsh, P. J.; Gordon, K. C.; Officer, D. L.; Campbell, W. M. *J. Mol. Struct.: THEOCHEM* **2006**, *759*, 17.
(33) Walsh, P. J.; Gordon, K. C.; Wagner, P.; Officer, D. L. *ChemPhysChem* **2006**, *7*, 2358.
(34) Howell, S. L.; Gordon, K. C.; Waterland, M. R.; Leung, K. H.; Phillips, D. L. *J. Phys. Chem. A* **2006**, *110*, 11194.
(35) Lundin, N. J.; Blackman, A. G.; Gordon, K. C.; Officer, D. L. *Angew. Chem., Int. Ed.* **2006**, *45*, 2582.
(36) Howell, S. L.; Scott, S. M.; Flood, A. H.; Gordon, K. C. *J. Phys. Chem. A* **2005**, *109*, 3745.
(37) McCreery, R. L. *Raman Spectroscopy for Chemical Analysis*; John Wiley & Sons, Inc: New York, 2000.
(38) Myers, A. B.; Li, B.; Ci, X. *J. Chem. Phys.* **1988**, *89*, 1876.
(39) Foster, C. E.; Barham, B. P.; Reid, P. J. *J. Chem. Phys.* **2001**, *114*, 8492.
(40) Becke, A. D. *J. Chem. Phys.* **1993**, *98*, 5648.
(41) Lee, C.; Yang, W.; Parr, R. G. *Phys. Rev. B* **1988**, *37*, 785.
(42) Frisch, M. J.; Trucks, G. W.; Schlegel, H. B.; Scuseria, G. E.; Robb, M. A.; Cheeseman, J. R.; Montgomery J. A., Jr.; Vreven, T.; Kudin, K. N.; Burant, J. C.; Millam, J. M.; Iyengar, S. S.; Tomasi, J.; Barone, V.; Mennucci, B.; Cossi, M.; Scalmani, G.; Rega, N.; Petersson, G. A.; Nakatsuji, H.; Hada, M.; Ehara, M.; Toyota, K.; Fukuda, R.; Hasegawa, J.; Ishida, M.; Nakajima, T.; Honda, Y.; Kitao, O.; Nakai, H.; Klene, M.; Li, X.; Knox, J. E.; Hratchian, H. P.; Cross, J. B.; Bakken, V.; Adamo, C.; Jaramillo, J.; Gomperts, R.; Stratmann, R. E.; Yazyev, O.; Austin, A. J.; Cammi, R.; Pomelli, C.; Ochterski, J. W.; Ayala, P. Y.; Morokuma, K.; Voth, G. A.; Salvador, P.; Dannenberg, J. J.; Zakrzewski, V. G.; Dapprich, S.; Daniels, A. D.; Strain, M. C.; Farkas, O.; Malick, D. K.; Rabuck, A. D.; Raghavachari, K.; Foresman, J. B.; Ortiz, J. V.; Cui, Q.; Baboul, A. G.; Clifford, S.; Cioslowski, J.; Stefanov, B. B.; Liu, G.; Liashenko, A.; Piskorz, P.; Komaromi, I.; Martin, R. L.; Fox, D. J.; Keith, T.; Al.Laham, M. A.; Peng, C. Y.; Nanayakkara, A.; Challacombe, M.; Gill, P. M. W.; Johnson, B.; Chen, W.; Wong, M. W.; Gonzalez, C.; Pople, J. A. Gaussian 03W, versions B04 and C02; Gaussian, Inc.: Wallingford, CT, 2004.
(43) Walsh, P. J.; Gordon, K. C.; Lundin, N. J.; Blackman, A. G. *J. Phys. Chem. A* **2005**, *109*, 5933.
(44) Durig, J. R.; Xiao, J.; Robb, J. B., II; Daeyaert, F. F. D. *J. Raman Spectrosc.* **1998**, *29*, 463.
(45) Mohamed, T. A.; Guirgis, G. A.; Nashed, Y. E.; Durig, J. R. *Vib. Spectrosc.* **2002**, *30*, 111.
(46) Durig, J. R.; Guirgis, G. A.; Zheng, C.; Mohamed, T. A. *Spectrochim. Acta, Part A* **2003**, *59A*, 2099.
(47) Waterland, M. R.; Howell, S. L.; Gordon, K. C. *J. Phys. Chem. A* **2007**, *111*, 4604.
(48) Howell, S. L.; Gordon, K. C.; McGarvey, J. J. *J. Phys. Chem. A* **2005**, *109*, 2948.
(49) Lundin, N. J.; Walsh, P. J.; Howell, S. L.; Blackman, A. G.; Gordon, K. C. *Chem.—Eur. J.* **2008**, *14*, 11573.
(50) Schaftenaar, G.; Noordik, J. H. *J. Comput.-Aided Mol. Des.* **2000**, *14*, 123.
(51) Heller, E. J. *J. Chem. Phys.* **1975**, *62*, 1544.
(52) Heller, E. J. *Faraday Discuss. Chem. Soc.* **1983**, 141.
(53) Heller, E. J.; Sundberg, R.; Tannor, D. *J. Phys. Chem.* **1982**, *86*, 1822.

(54) Myers, A. B. Excited electronic state properties from ground-state resonance Raman intensities. In *Laser Techniques in Chemistry*; Myers, A. B., Rizzo, T. R., Eds.; John Wiley & Sons, Inc: New York, 1995; Vol. XXIII, p 325.
(55) Li, B.; Johnson, A. E.; Mukamel, S.; Myers, A. B. *J. Am. Chem. Soc.* **1994**, *116*, 11039.
(56) Alfonso, M.; Stoeckli-Evans, H. *Acta Crystallogr., Sect. E* **2001**, *E57*, o242.
(57) Piglosiewicz, I. M.; Beckhaus, R.; Saak, W.; Haase, D. *J. Am. Chem. Soc.* **2005**, *127*, 14190.
(58) Du, M.; Bu, X.-H.; Biradha, K.; Shionoya, M. *J. Chem. Res.* **2002**, 493.
(59) Bu, X.-H.; Biradha, K.; Yamaguchi, T.; Nishimura, M.; Ito, T.; Tanaka, K.; Shionoya, M. *Chem. Commun.* **2000**, 1953.
(60) Bates, C. G.; Saejueng, P.; Murphy, J. M.; Venkataraman, D. *Org. Lett.* **2002**, *4*, 4727.
(61) Kirchhoff, J. R.; McMillin, D. R.; Robinson, W. R.; Powell, D. R.; McKenzie, A. T.; Chen, S. *Inorg. Chem.* **1985**, *24*, 3928.
(62) Okubo, T.; Kitagawa, S.; Kondo, M.; Matsuzaka, H.; Ishii, T. *Angew. Chem., Int. Ed.* **1999**, *38*, 931.
(63) Catalano, V. J.; Wayne, E.; Larson Olmstead, M. M.; Gray, H. B. *Inorg. Chem.* **1994**, *33*, 4502.
(64) Burke, K.; Werschnik, J.; Gross, E. K. U. *J. Chem. Phys.* **2005**, 123.
(65) Dreuw, A.; Head-Gordon, M. *J. Am. Chem. Soc.* **2004**, *126*, 4007.
(66) Fink, R. F.; Pfister, J.; Zhao, H. M.; Engels, B. *Chem. Phys.* **2008**, *346*, 275.
(67) Berger, R. M.; McMillin, D. R. *Inorg. Chim. Acta* **1990**, *177*, 65.
(68) Maruszewski, K.; Bajdor, K.; Strommen, D. P.; Kincaid, J. R. *J. Phys. Chem.* **1995**, *99*, 6286.
(69) Myers, A. B. *Chem. Rev.* **1996**, *96*, 911.
(70) Bradley, P. G.; Kress, N.; Hornberger, B. A.; Dallinger, R. F.; Woodruff, W. H. *J. Am. Chem. Soc.* **1981**, *103*, 7441.
(71) Treadway, J. A.; Loeb, B.; Lopez, R.; Anderson, P. A.; Keene, F. R.; Meyer, T. J. *Inorg. Chem.* **1996**, *35*, 2242.
(72) Blaskie, M. W.; McMillin, D. R. *Inorg. Chem.* **1980**, *19*, 3519.
(73) McMillin, D. R.; Kirchhoff, J. R.; Goodwin, K. V. *Coord. Chem. Rev.* **1985**, *64*, 83.
(74) Cuttell, D. G.; Kuang, S.-M.; Fanwick, P. E.; McMillin, D. R.; Walton, R. A. *J. Am. Chem. Soc.* **2002**, *124*, 6.

JP808179M